Nano-Micro Letters

e-ISSN 2150-5551
CN 31-2103/TB

ARTICLE

https://doi.org/10.1007/s40820-022-00946-x

Cite as
Nano-Micro Lett.
(2022) 14:204

Received: 17 August 2022
Accepted: 17 September 2022

High-Performance Perovskite Quantum Dot Solar Cells Enabled by Incorporation with Dimensionally Engineered Organic Semiconductor

Seyeong Lim[1], Dae Hwan Lee[1], Hyuntae Choi[1], Yelim Choi[1], Dong Geon Lee[2,3], Sung Beom Cho[3,4], Seonkyung Ko[5], Jongmin Choi[5] ✉, Younghoon Kim[6] ✉, Taiho Park[1] ✉

HIGHLIGHTS

- We designed and developed a 3D star-shaped conjugated molecule (Star-TrCN) to incorporate organic semiconductor with $CsPbI_3$ perovskite quantum dots (PQDs).
- The robust chemical bonding of Star-TrCN and PQDs is demonstrated by theoretical modeling and experimental validation, which significantly improved the cubic-phase stability of $CsPbI_3$-PQDs by passivating vacant sites and preventing moisture penetration.
- The Star-PQD hybrid solar cells not only achieved remarkable device stability over 1000 h at 20–30% relative humidity, but also boosted power conversion efficiency up to 16.0% via cascade energy band structure.

ABSTRACT Perovskite quantum dots (PQDs) have been considered promising and effective photovoltaic absorber due to their superior optoelectronic properties and inherent material merits combining perovskites and QDs. However, they exhibit low moisture stability at room humidity (20–30%) owing to many surface defect sites generated by inefficient ligand exchange process. These surface traps must be re-passivated to improve both charge transport ability and moisture stability. To address this issue, PQD-organic semiconductor hybrid solar cells with suitable electrical properties and functional groups might dramatically improve the charge extraction and defect passivation. Conventional organic semiconductors are typically low-dimensional (1D and 2D) and prone to excessive self-aggregation, which limits chemical interaction with PQDs.

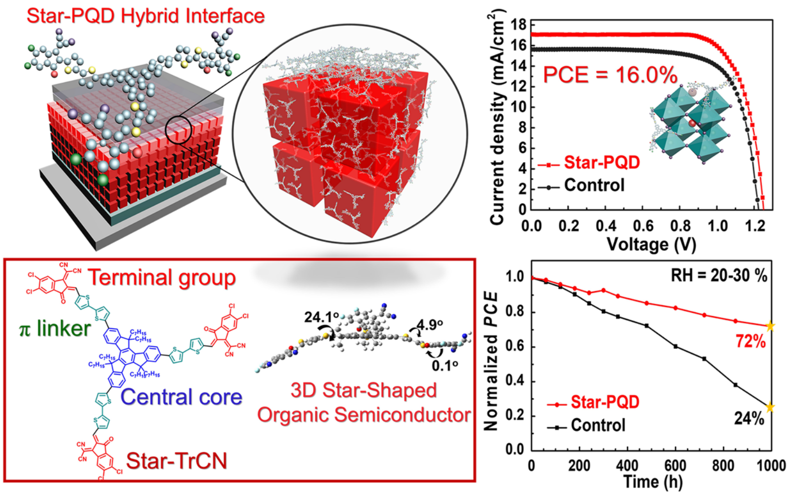

Seyeong Lim and Dae Hwan Lee contributed equally to this work.
✉ Jongmin Choi, whdals1062@dgist.ac.kr; Younghoon Kim, younghoon.kim@kookmin.ac.kr; Taiho Park, taihopark@postech.ac.kr
[1] Department of Chemical Engineering, Pohang University of Science and Technology (POSTECH), Pohang 37673, Republic of Korea
[2] Department of Materials Science and Engineering, Hanyang University, Seoul 04763, Republic of Korea
[3] Center of Materials Digitalization, Korea Institute of Ceramic Engineering and Technology (KICET), Jinju 52851, Republic of Korea
[4] Department of Materials Science and Engineering, Ajou University, Suwon 16499, Republic of Korea
[5] Department of Energy Science and Engineering, Daegu Gyeongbuk Institute of Science and Technology (DGIST), Daegu 42988, Republic of Korea
[6] Department of Chemistry, Kookmin University, Seoul 02707, Republic of Korea

In this work, we designed a new 3D star-shaped semiconducting material (Star-TrCN) to enhance the compatibility with PQDs. The robust bonding with Star-TrCN and PQDs is demonstrated by theoretical modeling and experimental validation. The Star-TrCN-PQD hybrid films show improved cubic-phase stability of $CsPbI_3$-PQDs via reduced surface trap states and suppressed moisture penetration. As a result, the resultant devices not only achieve remarkable device stability over 1000 h at 20–30% relative humidity, but also boost power conversion efficiency up to 16.0% via forming a cascade energy band structure.

KEYWORDS $CsPbI_3$ quantum dots; Star-shaped organic semiconductors; Hybrid perovskite quantum dots; Solar cell stability; High-efficiency photovoltaics

1 Introduction

Organic–inorganic hybrid perovskite solar cells (PSCs) have shown remarkable device performance. Through optimizing the compositional alloying, post-processing step, interfacial engineering and device architecture [1–5], researchers have increased the power conversion efficiency (PCE) of PSCs to above 25% [6]. However, the long-term stability of PSCs is limited by degradation of the perovskite absorbers [7, 8]. Under operational circumstances (i.e., high temperature or humidity), hybrid perovskites decompose into PbI_2. Moreover, the organic compounds used as the monovalent cations of the perovskite structure (ABX_3) (e.g., methylammonium, ethylammonium and formamidinium) are volatile, reducing the device stability [9].

Recently, replacing the organic cation (the A site of ABX_3) with an inorganic cation has been regarded as a facile strategy for improving the stability of PSCs [10–12]. Among these all-inorganic PSCs, $CsPbI_3$ is a most promising photovoltaic absorber because its bandgap ($E_g = 1.73$ eV) is appropriate for the single-junction solar cell applications [13]. However, the photoactive cubic-phase $CsPbI_3$ (α-$CsPbI_3$) tends to transform into the more thermodynamically stable non-photoactive phase (δ-$CsPbI_3$) below 320 °C [14].

Luther and co-workers proposed a perovskite quantum dot (PQD) strategy to overcome the cubic-phase instability issues of bulk $CsPbI_3$ [15]. The cubic-phase stability of $CsPbI_3$ is much higher in PQDs than in bulk perovskites because the surface strain increases according to the decreases in the crystal size of perovskites with surface ligand stabilization [16]. Moreover, $CsPbI_3$-PQDs exhibit superior optical and electronic properties such as size-tunable E_g, high photoluminescence quantum yield, high absorption coefficient and high charge carrier mobility [17, 18]. Consequently, the $CsPbI_3$-PQDs have been considered promising and effective photovoltaic absorbers [19, 20].

Although $CsPbI_3$-PQDs exhibit outstanding photovoltaic properties, their moisture stability should be further improved. In the PQD synthetic process, the PQDs have been stabilized with long-chain hydrocarbon ligands such as oleic acid and oleylamine (OLA) [21, 22]. Native ligands enhance the colloidal stability of PQDs [13, 23, 24], but their insulating properties prevent efficient charge transport. To enhance the electronic coupling within PQDs, the long-chain ligands should be replaced with short ligands (e.g., acetate) through the solid-state ligand exchange process [13, 25]. Although the ligand exchange process increases the charge transport ability in PQD films [26, 27], the inefficient ligand exchange can induce surface trap states of the PQDs [28]. Moreover, under the device operating conditions, moisture can penetrate the PQDs through the surface defect sites, causing the PQD damage, low device performance and stability [29]. The most widely used hole transport material (HTM) in high-efficiency PQD solar cells is a spiro-OMeTAD, which requires dopants [e.g., lithium salt (Li-TFSI) and cobalt complexes (FK209)] that easily absorb moisture and accelerate the degradation of the device stability [30, 31].

To improve the moisture stability of PQDs, several researchers have attempted to combine PQDs with organic conjugated molecules, forming hybrid PQDs (HPQDs) [29, 32–34]. The organic conjugated molecules not only provide a physical hydrophobic barrier to prevent moisture penetration of HPQDs, but also passivate the surface defects through their various functional groups (e.g., –COO, –CN and halide) [35]. Ma et al. [33] and Hu et al. [36] reported that the charge collection efficiency in PQD devices can be significantly enhanced with hybrid configurations (e.g., HTM and hetero-interface architectures), highlighting the advantages of HPQDs. Even though typical low-dimensional [i.e., one- and two-dimensional (1D and 2D, respectively)] organic semiconductors (e.g., polymers and fused-ring

https://doi.org/10.1007/s40820-022-00946-x

small molecules) show high efficiency in organic-based optoelectronics owing to their excellent crystalline properties, charge carrier extraction from the PQDs to the organic semiconductors is inefficient for the HPQD system due to the large difference in their surface energies [17]. Further, the low-dimensional organic semiconductors are prone to excessive self-aggregation, resulting in poor interaction with PQDs [37]. Therefore, a new organic semiconductor design is required to enhance the compatibility between organic semiconductors and PQDs.

Here, considering the dimensionality in engineering organic semiconductors, a newly designed and synthesized three-dimensional (3D) star-shaped semiconductor (Star-TrCN) is combined with $CsPbI_3$-PQDs to develop a successful HPQD system. The distinctive structure of star-shaped semiconductors could provide tunable energy levels, high charge carrier mobility and isotropic charge transfer abilities in contrast to 1D semiconductors. Therefore, the Star-TrCN is employed as the interlayer between the HTM and PQDs, and is expected to simultaneously improve the device performance and stability of PQD solar cells. This core structure [10,15-dihydro-5H-diindeno[1,2-a;1′,2′-c] fluorene (truxene)] is facilely synthesized and undergoes high π-conjugation with fluorene, thus facilitating charge transport [38–40]. Star-TrCN is designed by adjusting the energy level between the PQD and HTM layers in density functional theory (DFT) calculations. Truxene with a fused-ring aromatic structure confers hydrophobic properties to the upper layer of PQDs, preventing moisture penetration. Furthermore, the twisted structure of 3D star-shaped Star-TrCN more significantly suppresses self-aggregation than the linear structures of 1D molecule, increasing the compatibility between organic semiconductors and PQDs. Owing to these unique characteristics, 3D star-shaped structures have been discussed as efficient passivator of perovskite surface defects, improving the operational device performance in multiple ways [2, 41–43]. Star-TrCN also possesses several functional groups (–CO, –Cl and –CN) that can passivate the surface defects and result in chemical bonding with PQDs. The Star-PQD hybrid film significantly enhances the cubic-phase stability by passivating the surface defects and preventing moisture penetration through the hygroscopic metal complex dopants in HTM (Spiro-OMeTAD). In long-term stability tests, Star-PQD-based solar cells retained 72% of their initial PCE at ambient conditions (20–30% RH) even after 1000 h. The cascade energy level structure further improves the charge extraction, achieving 16.0% PCE. The 3D star-shaped organic semiconductor design promises the simultaneous improvement of the stability and efficiency of HPQD-based solar cells.

2 Experimental

2.1 Materials

All the organic chemicals and solvents were purchased from Sigma-Aldrich and Alfa Aesar and used directly without further purification. Lead iodide (PbI_2), 1-octadecene (ODE), oleic acid (OA), cesium carbonate (Cs_2CO_3), n-hexane, n-octane and lithium bis(trifluoromethylsulfonyl)imide (Li-TFSI) were purchased from Alfa Aesar. Oleylamine (OLA), sodium acetate (NaOAc), chlorobenzene (CB), chloroform (CF), acetonitrile (AN), methyl acetate (MeOAc) and ethyl acetate (EtOAc) were purchased from Sigma-Aldrich. Phenethylammonium iodide (PEAI) was purchased from GreatcellSolar. TiO_2 precursor solution (SC-BT060) and 2 M $TiCl_4$ aqueous solution were purchased from Sharechem. 2,20,7,70-Tetrakis(N,N-di-p-methoxyphenylamine)-9,90-spirobifluorene (Spiro-OMeTAD) was purchased from Lumtec. 2-Amylpyridine was purchased from TCI.

2.2 Synthesis of Cs-oleate Solution

Cs_2CO_3 (0.407 g), ODE (20 mL) and OA (1.25 mL) were added to a 250-mL three-necked flask. The system was vacuumed at 120 °C for 0.5 h under stirring. Then, N_2 was introduced into the system and the solution was stored at this condition before injection.

2.3 Synthesis of $CsPbI_3$-PQDs

PbI_2 (0.5 g) and ODE (25 mL) were added to a 100-mL three-necked flask. The system was vacuumed at 120 °C for 30 min. Then, OA (2.5 mL) and OLA (2.5 mL) were added to the system, and the system was vacuumed at 120 °C for 0.5 h. Thereafter, N_2 was introduced into the system and heated to 180 °C. At 180 °C, Cs-oleate (2 mL) was quickly injected to the system, and the system was cooled after 10 s to room temperature under ice-water bath.

2.4 Purification of $CsPbI_3$-PQDs

$CsPbI_3$-PQD solution was purified through two steps. In the first step, MeOAc (30 mL) was added to 15 mL of $CsPbI_3$-PQD crude solution. The system was centrifuged at 5 krpm for 3 min. Then, the as-prepared $CsPbI_3$-PQD precipitate was dispersed n-hexane (5 mL). In the second step, MeOAc (7 mL) was added to the system. The system was centrifuged at 5000 rpm for 3 min. Then, as-prepared $CsPbI_3$-PQD precipitate was dispersed n-hexane (15 mL). The solution was centrifuged at 5 krpm for 3 min. Thereafter, the purified $CsPbI_3$-PQD solution was collected. Finally, this solution was dried under vacuum, and the achieved $CsPbI_3$-PQD solid was dispersed in n-octane (75 mg mL^{-1}). The size of the synthesized PQDs was approximately 10–12 nm (Fig. S1).

2.5 Fabrication of $CsPbI_3$-PQD Solar Cells

The c-TiO_2 electron transport layer was spin-coated on the FTO substrates at 3 krpm for 0.5 min, and the substrates were annealed at 500 °C for 1 h. After the substrates cooled to room temperature, the substrates were immersed in $TiCl_4$ aqueous solution (120 mM) at 70 °C for 1 h. Then, they were washed by deionized water and annealed at 500 °C for 1 h. The $CsPbI_3$-PQD solution (75 mg mL^{-1} in n-octane) was spin-coated onto the c-TiO_2 deposited substrates at 1 krpm for 20 s followed by 2 krpm for 5 s. The $CsPbI_3$-PQD film was immersed in ligand solution of NaOAc in MeOAc (1 mg mL^{-1}) and spin-dried. Thereafter, the ligand-exchanged $CsPbI_3$-PQD film was washed by MeOAc for washing. The step was repeated for 5 times to achieve optimum thickness (~ 250 nm). Subsequently, thick $CsPbI_3$-PQD film was immersed in ligand solution of PEAI in EtOAc (1 mg mL^{-1}) and spin-dried. After that, for Star-TrCN treatment, thick $CsPbI_3$-PQD film was soaked in Star-TrCN solution in CF (1 mg mL^{-1}) for 5 s and spin-dried. The spiro-OMeTAD hole transport layer was prepared by mixing spiro-OMeTAD (72.3 mg), CB (1 mL), 2-amylpyridine (28.7 μL) and 17.6 μL of Li-TFSI solution in AN (520 mg mL^{-1}). This solution was spin-coated on the thick $CsPbI_3$-PQD film at 4 krpm for 30 s. Finally, top electrodes (MoO_x and Ag with thicknesses of 15 and 120 nm) were deposited by using thermal evaporation equipment.

2.6 Characterization

Cyclic voltammetry (CV) analyses were carried out witha CHI 600C potentiostat (CH Instruments) at a scan rate of 100 mV s^{-1} in 0.1 M solution of tetrabutylammonium perchlorate in acetonitrile. Cross-sectional scanning electron microscopy (SEM) image of $CsPbI_3$-PQD solar cell was acquired by using a Hitachi SU8230 equipment. UV–Vis absorption spectra of $CsPbI_3$-PQD films were measured by employing a Shimadzu UV-2600 spectrophotometer. X-ray photoelectron spectra (XPS) spectra were measured by using a Thermo Scientific ESCALAB 250Xi analyzer. For preparing grazing-incidence small-angle X-ray scattering (GIWAXS) samples, 1 by 1 cm^2 silicon wafers were used as substrates. Solutions (Star-TrCN, ITIC, Y6, PBDB-T, $CsPbI_3$-PQD and Star-PQD) were spin-coated on the substrates. The GIWAXS analysis was conducted at the Pohang Accelerator Laboratory (beamline 9A, Republic of Korea) with incidence angles between 0.1 and 0.3°. X-ray diffraction (XRD) patterns were measured by using a Bruker D2 Phaser diffractometer. Photoluminescence (PL) spectra of $CsPbI_3$-PQD films were measured by employing a Horiba Scientific Flouromax-4 spectrophotometer. Time-resolved PL (TRPL) decay curves of $CsPbI_3$-PQD films were measured by employing a Hamamatsu Quantaurus-Tau C11367 spectrometer. The $J-V$ curves, light intensity-dependent V_{OC} and stable power output were acquired by using a Newport Oriel Sol 3A solar simulator equipped with a 450 W Xe lamp and a Keithley 2400 sourcemeter under a simulated air-mass 1.5 global spectrum at 100 mW cm^{-2}. External quantum efficiency (EQE) spectra of $CsPbI_3$-PQD solar cells were measured by employing a Newport Oriel QuantX-300 incident photon-to-current efficiency (IPCE) equipment with an Oriel Cornerstone 130 monochromator. DFT calculations with the B3LYP/6-31G (d, p) basis set were performed utilizing Gaussian 09 to evaluate the molecular conformations and electrostatic potential. In particular, alkyl chains were replaced with a methyl or isobutyl group to simplify the calculations and reduce the computational time. Depth profiling of PQD solar cells was analyzed by time-of-flight secondary ion mass spectrometry (ToF-SIMS) using

https://doi.org/10.1007/s40820-022-00946-x

ToF-SIMS IMS 6F equipped with Cs$^+$ Gun (impact energy: 5 keV, Current: 5 nA, Raster size: 300 × µm^2 and Analysis Area: 60 um(Φ)). Atom force microscopy (AFM) images of CsPbI$_3$-PQD films were measured by employing a Park System NX10 microscope.

3 Results and Discussion

3.1 Design Strategy of Star-TrCN Incorporated CsPbI$_3$-PQD Solar Cells

The chemical structure and synthetic routes of Star-TrCN are shown in Fig. 1a and Scheme S1. The detailed synthetic procedures and characterizations are provided in the supporting information. The synthesis of the star-shaped semiconductors targets a truxene core with three fluorine units sharing a central benzene ring. To obtain an adequate energy level and modulate the twisted 3D structure, truxene was expanded by a linker with bi-thiophene through the Suzuki cross-coupling reaction and attached to the terminal group via Knoevenagel condensation. The chemical structures of the intermediates and final molecules were confirmed by ^{1}H-, ^{13}C-NMR, matrix-assisted laser desorption time-of-flight mass (MALDI-TOF-MS) spectrometry and an elemental analysis (EA) (Figs. S2–S4). During the synthesis, the core, linker and terminal group of Star-TrCN were finely controlled to modulate the energy levels of HTM and the PQDs. The resulting Star-TrCN was characterized by cyclic voltammetry and ultraviolet–visible (UV–Vis) absorption spectroscopy (Fig. S5). The highest occupied and lowest unoccupied molecular orbital energy levels of Star-TrCN were calculated to be − 5.38 and − 3.28 eV, respectively. The cascade formation using Star-TrCN for interfacial energy level alignment improved the charge extraction between PQDs and HTM (Fig. 1b). Moreover, their multiple aromatic ring structures provide superior hydrophobic properties to the PQDs (Fig. 1c). The excellent hydrophobicity of these structures effectively prevents moisture penetration. Figure 1d shows a schematic

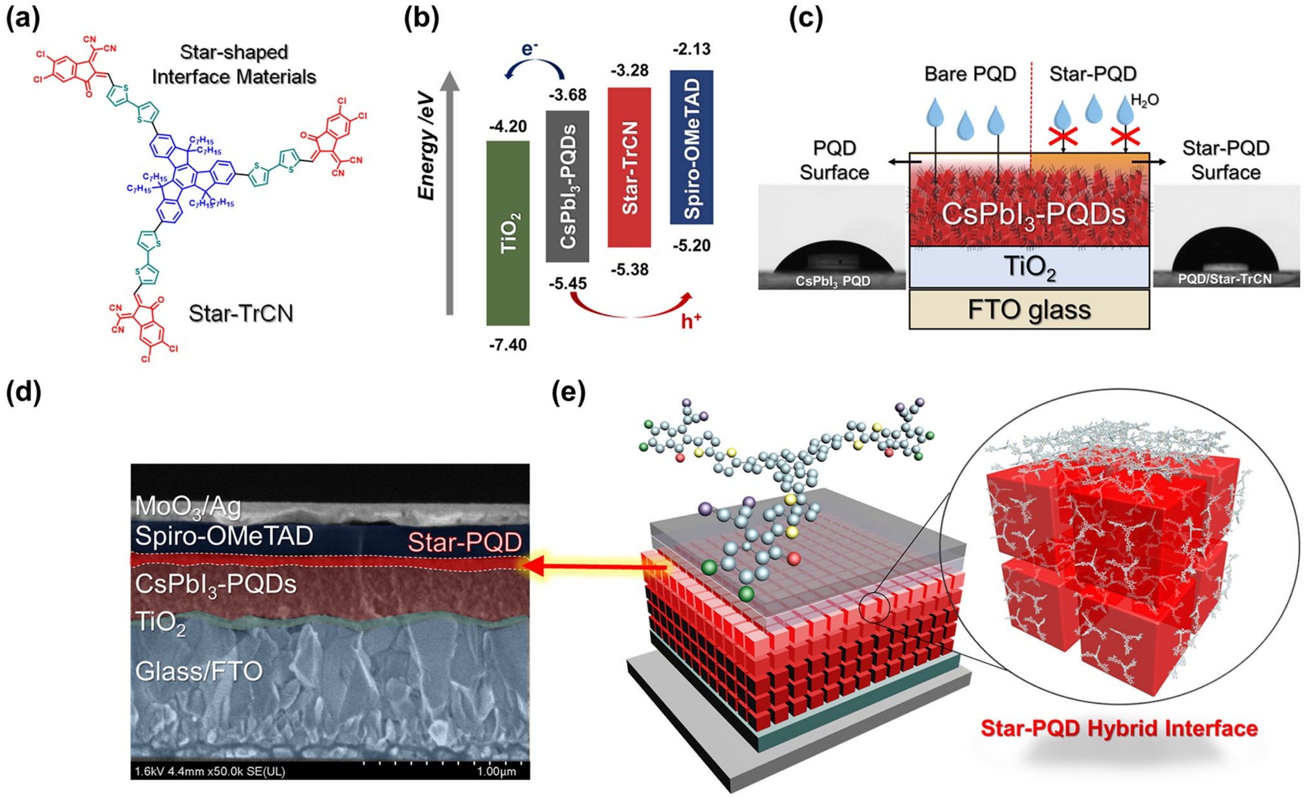

Fig. 1 **a** Chemical structure of Star-TrCN. **b** Energy level diagram of charge transfer between CsPbI$_3$-PQDs and each transport layer. **c** Schematic showing moisture penetration impedance of the Star-PQD formation. **d** Cross-sectional SEM image of the fabricated device and the device architecture with Star-PQD hybrid interfaces. **e** Schematic of the architecture of PQD solar cells with a Star-PQD hybrid interface

and a cross-sectional SEM image of the $CsPbI_3$-PQD solar cells. The device was fabricated through solid-state ligand exchange of $CsPbI_3$-PQDs, which preserves the original crystal size of the PQDs, onto the electron-transporting material (compact TiO_2). After sequentially depositing the PQDs, the Star-TrCN interface layer was spin-coated on the top PQD surfaces to form Star-PQD hybrid films. Finally, spiro-OMeTAD was spin-coated as an HTM, followed by sequential deposition of MoO_x and Ag (see the Experimental Section for details) (Fig. 1e).

The Star-TrCN is dissolved in volatile organic solvents [e.g., chloroform (CF), chlorobenzene (CB)] and, as shown in the experimental section, we dissolved Star-TrCN in CF and spin-coated onto the PQD films to form the Star-PQD layer. However, the spiro-OMeTAD is also dissolved in the same organic solvents, which can damage on Star-TrCN layer during spiro-OMeTAD deposition. Although the Star-TrCN layer could be flushed away after spiro-OMeTAD deposition, there is a solvent resistance to CB because the Star-TrCN penetrates into the PQD layer and can strongly result in the chemical bonding with the PQD. We confirmed the robust solvent resistance of Star-PQD film using UV–Vis and nanoscale Fourier transform infrared (nano-FTIR) spectroscopy measurements. When the PQD film was treated with Star-TrCN, the proportion of Star-TrCN absorption range (i.e., 400–550 nm, Fig. S5c) was increased from that of bare PQD. Next, the Star-PQD films were flushed with CB solvent as done in the HTM spin coating process. The flushing process did not significantly affect the absorbance spectrum. In addition, we also performed nano-FTIR spectroscopy measurement. The nano-FTIR can visually show the presence of Star-TrCN depending on the intensity of its functional group [44]. As shown Fig. S6, the FTIR spectrum of the Star-TrCN showed a peak at 1500–1700 cm^{-1}, which is related to the stretching of C–C bonds in the aromatic ring of Star-TrCN. In the amplitude image, reflecting the topological information, we can observe the distribution of Star-TrCN. Similarly, the phase image also indicated the wide distribution of Star-TrCN, which shows that Star-TrCN was well incorporated into the PQDs as an interfacial material following the HTM deposition process (CB solvent).

3.2 Chemical Interaction Between Star-TrCN and $CsPbI_3$-PQDs

We performed DFT-based optimized structure, molecular dynamic modeling and X-ray photoelectron spectroscopy (XPS) measurements to clarify this robust interaction between PQDs and Star-TrCN. According to the results of the DFT calculation (Fig. 2a, c), In the ESP analysis, Star-TrCN exhibited negative potential in the edge regions because of a strong electron lone pair existing at the terminal unit (–CO, –CN and –Cl). The negative potentials and distorted 3D star-shaped structure effectively can passivate the surface defects of the PQDs. In particular, substantial negative potential of Star-TrCN could form a chemical bond with the PQD surface. To verify this chemical bond, we constructed the PQD slabs and simulated the adsorption behavior of the Star-TrCN. The $CsPbI_3$-PQD slab models are constructed using (001) surface that has two distinct terminations, CsI and PbI_2 [45]. Then, we modeled the adsorption behavior of Star-TrCN on the PQD surfaces with the segmented molecule with functional groups (–CO, –CN and –Cl) (Fig. S7). The adsorption energy is summarized in Table S1 using the equation $E_{Ads} = E_{total} - E_{slab} - E_{Star\text{-}TrCN}$. The most favorable configuration is –CN functional group of Star-TrCN on the Iodine vacancy of CsI termination with an adsorption energy of − 0.72 eV. Figure 2d shows the electron interaction between the two Cs atoms and –CN is the most significant. Since the iodine site is vacant, the –CN functional group directly interact with two Cs cations. The projected density of states of Cs and N atoms shows strong hybridization as shown in Fig. 2e, which indicates the covalent bond is formed between Cs ion and N atoms. This is consistent with the XPS core-level spectra in Star-PQD; the Cs $3d_{3/2}$ and Cs $3d_{5/2}$ signals were shifted to lower binding energies compared to those of the bare PQD film (by approximately 0.2 and 0.4 eV in the Cs $3d$ spectra, see Fig. 2f). This remarkable negative shift suggests the change of chemical bonding after Star-PQD films and the passivation effect of Star-TrCN, which is consistent with the DFT calculation. Furthermore, this Cs-N covalent bond can be plentiful considering the surface structure of PQDs. The CsI termination is more favoarble than PbI_2 termination [46], and iodine vacancy can be largely generated with its low vacancy formation energy of 0.38 eV. This means the –CN functional group of the Star-TrCN can be easily linked with the PQDs by forming the Cs-N covalent bonds.

3.3 Morphology Analysis of Star-TrCN Incorporated $CsPbI_3$-PQDs

Understanding the micromorphology of HPQD-type systems is crucial for comprehending the mechanism for

https://doi.org/10.1007/s40820-022-00946-x

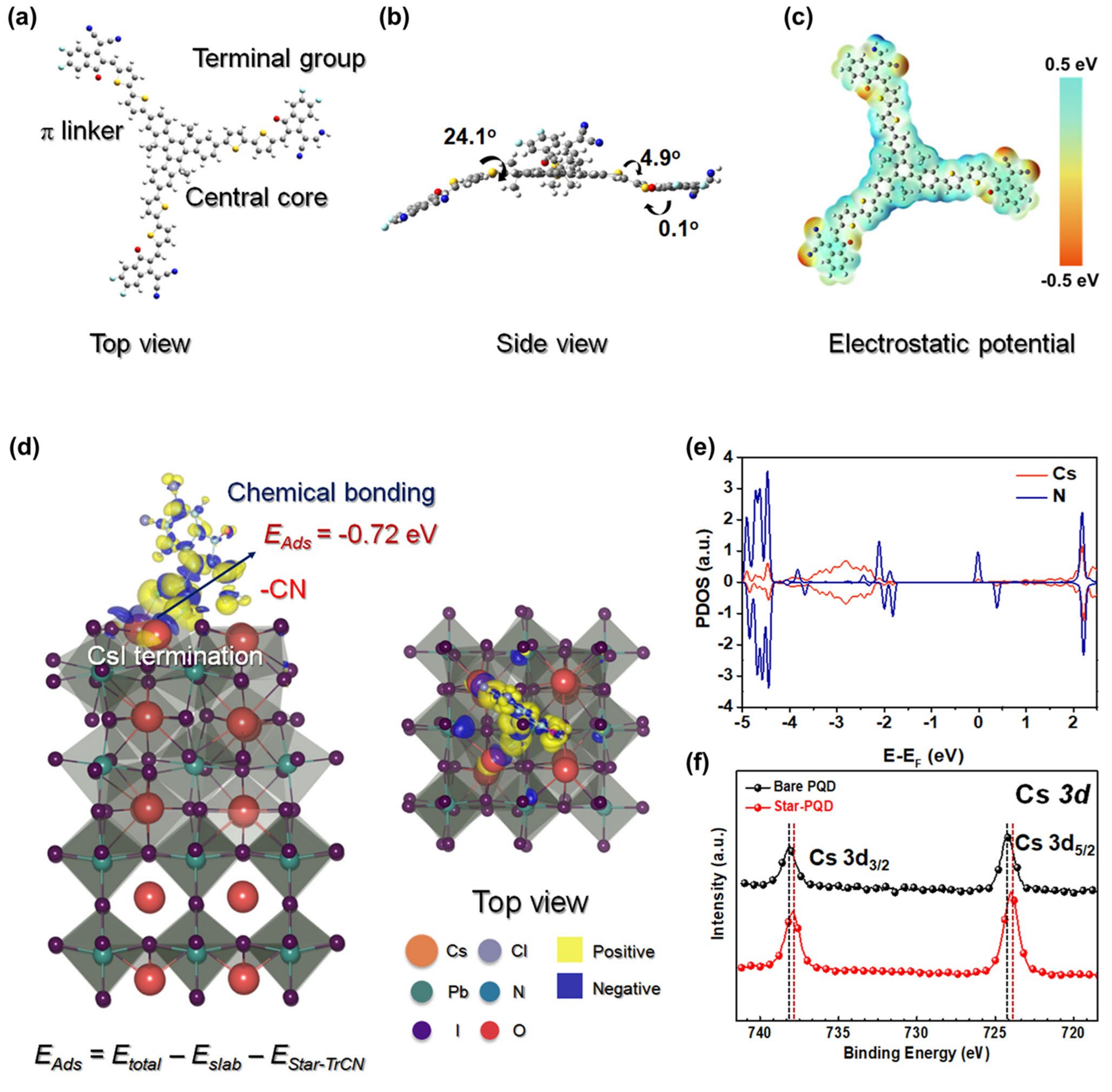

Fig. 2 **a** Optimized geometries, **b** dihedral angles and **c** electrostatic potential of the Star-TrCN using DFT calculation at B3LYP/6-31G (d, p) level. **d** Charge density difference with isosurface of 0.008 e $Å^{-3}$. **e** Projected density of states profiles of Cs and N ions for the most favorable adsorption configuration of Star-TrCN on the $CsPbI_3$-PQD surface (V_I-CN). **f** XPS Cs 3*d* core-level spectra of $CsPbI_3$-PQD films with and without Star-TrCN post-treatment

enhancing device performance. Therefore, we determined the crystal structure of each morphology from synchronous 2D GIWAXS and AFM measurements. Figure 3a shows the GIWAXS diffraction patterns of the $CsPbI_3$-PQD films in the bare and hybrid forms, respectively. Figure 3b shows the circular average profile of each film. The pristine $CsPbI_3$-PQD film presented strong X-ray characteristic diffraction peaks characterizing the (100), (110), (111), (200), (210), (211) and (220) planes of cubic-phase $CsPbI_3$. The pattern of the Star-PQD film was similar and the position

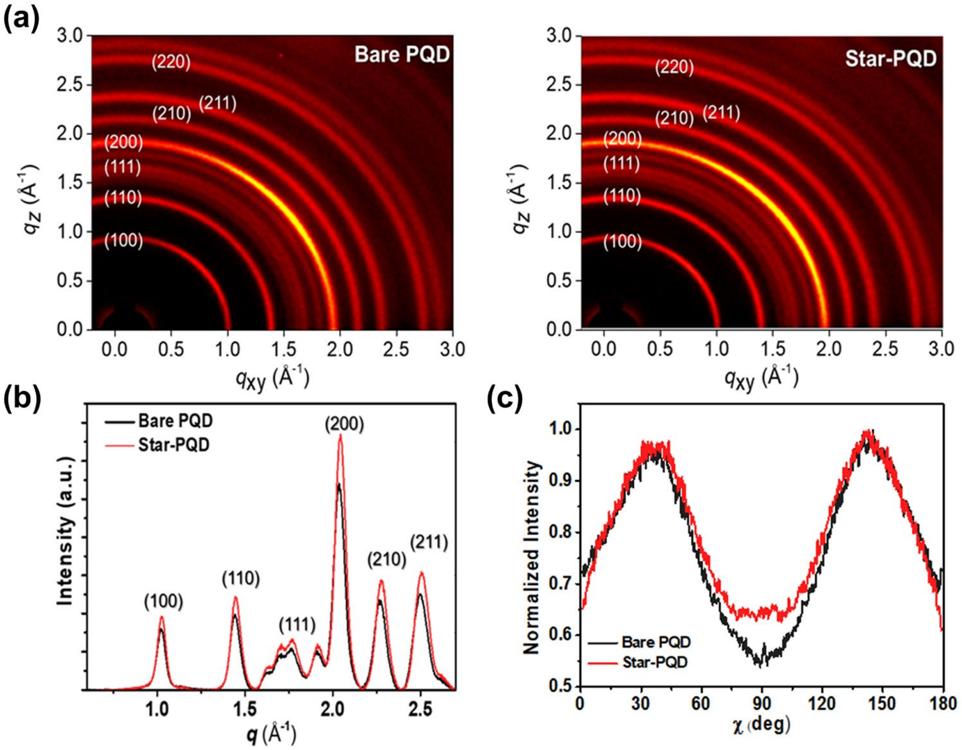

Fig. 3 **a** 2D-GIWAXS patterns, **b** azimuthally integrated profiles and **c** azimuthal angle scans of the (200) peaks in the GIWAXS patterns of the control $CsPbI_3$-PQD and Star-PQD hybrid films

of each diffraction peak was almost unchanged, suggesting that the cubic-phase of $CsPbI_3$-PQD was maintained after HPQD formation. In addition, the 2D diffraction peaks distributed along azimuthal angles between 0° and 180° along the ring at $q = 10$ nm^{-1}. Interestingly, the Star-PQD film featured a more ring-like diffraction pattern than the pristine $CsPbI_3$-PQD film (Fig. 3a). This morphological change indicates that the Star-TrCN contributed to increased random orientation in the PQD film via a strong molecular interaction between the Star-TrCN and the PQDs. The increased random orientation can enhance the charge transport along the multiple directions (Fig. 3c) [47, 48]. We also measured the GIWAXS of Star-TrCN neat films to investigate the correlation between their dimension and PQDs. In contrast to linear-type organic semiconductors (e.g., ITIC, Y6 and PBDB-T) with a strong crystal orientation in other HPQD systems, the Star-TrCN showed a disordered random orientation (Fig. S8) [20, 33, 49]. This imply amorphous morphology of Star-TrCN can facilitate the incorporation of PQDs [50, 51].

From the AFM measurements, we obtained the surface morphology of the PQD film in contact with the HTM. In contrast to the bare PQD film, the Star-PQD film showed an additional intermediate layer that apparently covered the surface of the PQD layer (Fig. S9). The increased surface roughness of the Star-PQD thin film was attributed to the amorphous property of Star-TrCN. Additionally, the hydrophobic organic layer formed on the PQD surface effectively suppressed the moisture penetration. To evaluate the change in surface hydrophobicity, we measured the contact angles of bare Star-TrCN, bare PQD, Star-PQD and spiro-OMeTAD films coated on a glass substrate (Fig. S10). The contact angles of the bare Star-TrCN and PQD films were 102.1° and 59.8°, respectively. When Star-TrCN was treated on the PQD solids after the ligand exchange process, the contact angle of Star-PQD film was measured as 87.3°, higher than that of bare PQD solids.

3.4 Cubic-Phase Stability of Star-TrCN Incorporated $CsPbI_3$-PQDs

Next, the elemental depth distribution in the integrated hybrid film was determined by time-of-flight secondary ion

https://doi.org/10.1007/s40820-022-00946-x

mass spectrometry (ToF-SIMS) (Fig. S11). The ToF-SIMS profiles of bare PQD and Star-PQD hybrid films detected the Pb and I ions constituting perovskite. Meanwhile, the simultaneous indication of C, N, S and Cl in the profile of the Star-PQD hybrid film confirmed the presence of Star-TrCN on the PQD surfaces. This indicated that the integrated Star-PQD layer was approximately 70–80 nm from the PQD surface, as shown in Fig. 1d, e. To confirm whether this integrated organic/PQD film practically contributed to the cubic-phase robustness of the $CsPbI_3$-PQDs film, we conducted aging tests of the bare PQD and Star-PQD films under ambient conditions with a 20%–30% relative humidity (RH) at room temperature. The difference in cubic-phase stability between the $CsPbI_3$-PQD films with and without the Star-TrCN treatment under ambient conditions was evaluated from X-ray diffraction (XRD) patterns of the two films (Fig. 4a). Initially, the spectra of both films exhibited the (100), (110) and (200) plane peaks of cubic-phase $CsPbI_3$-PQDs. After 30 days, the intensities of the cubic-phase peaks were almost preserved in the Star-PQD film but were significantly reduced (being replaced by new orthorhombic-phase peaks) in the bare PQD film. After 50 days, the intensities of the cubic-phase peaks of $CsPbI_3$-PQDs remained apparent in the Star-PQD film. This result indicated that Star-TrCN treatment significantly improves the cubic-phase stability of $CsPbI_3$-PQDs by preventing moisture-induced

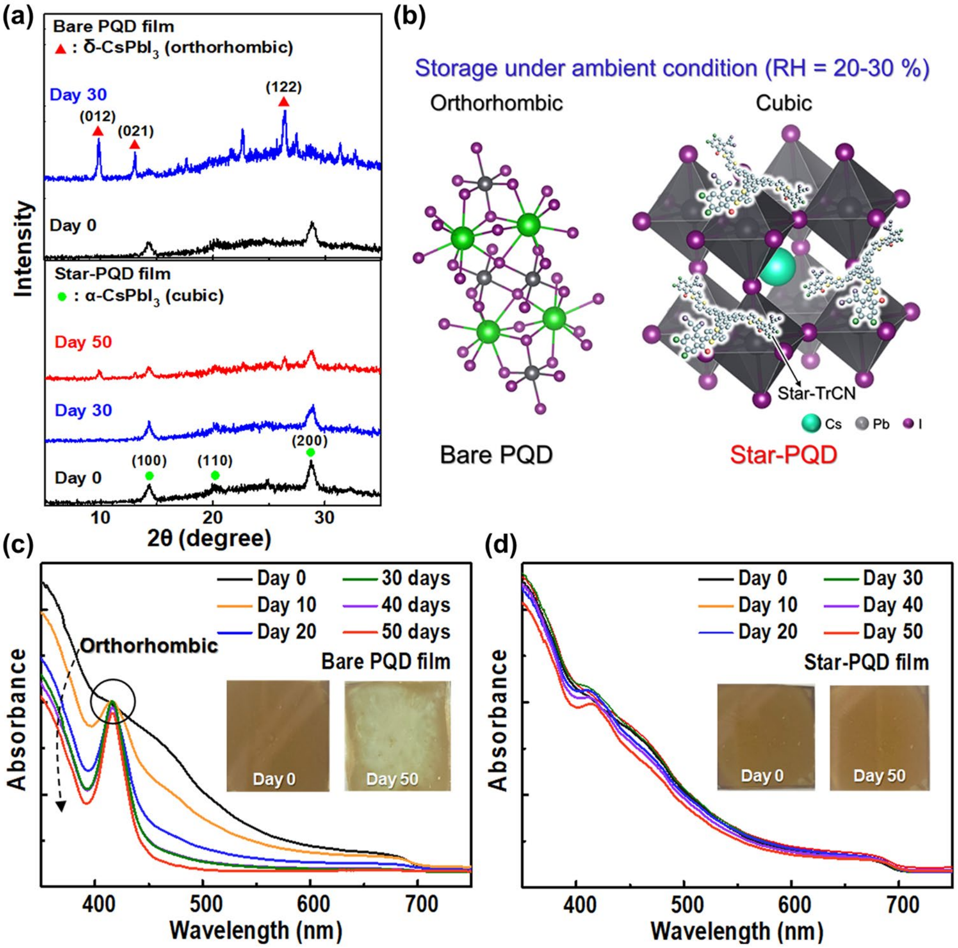

Fig. 4 **a** XRD patterns of the glass/bare PQD film and the glass/Star-PQD film before and after aging for 50 days under ambient conditions (20–30% RH). **b** Schematic showing the cubic-phase degradation of $CsPbI_3$-PQDs at 20–30% RH. UV–Vis absorption spectra of **c** glass/bare PQD film and **d** glass/Star-PQD film before and after aging for 50 days at 20–30% RH (Insets: film images before and after aging for 50 days at 20–30% RH)

hydration (Fig. 4b). Similarly, the UV–Vis absorbance of the bare PQD film was significantly reduced after aging for 20 days (Fig. 4c), whereas that of the Star-PQD film was highly preserved without any reduction even after aging for 50 days (Fig. 4d). As shown in photographic images (inset images in Fig. 4c, d), the Star-PQD film maintained its initial brownish color for 50 days under ambient conditions. However, the bare PQD film became yellowish and then transparent after 50 days (Fig. S12), implying that the cubic-phase of the $CsPbI_3$-PQDs was completely transformed to the orthorhombic phase. In other words, the cubic-phase stability of $CsPbI_3$-PQDs was much higher in the Star-PQD film than in the bare PQD film.

3.5 Photophysical Properties and Photovoltaic Performance

To investigate the dynamic charge carrier transfer behavior after Star-TrCN treatment on PQDs, we carried out steady-state PL and TRPL measurements. As shown in Fig. 5a, the Star-PQD films showed more remarkable emission quenching than the bare PQD film, suggesting that they can achieve effective hole extraction. In addition, the Star-PQD films showed blueshift of the PL peak at 686–683 nm. This blueshift indicates the defect passivation effect of the Star-TrCN [41, 42]. The PL decay curves in Fig. 5b were fitted by a bi-exponential decay function and the detailed parameters

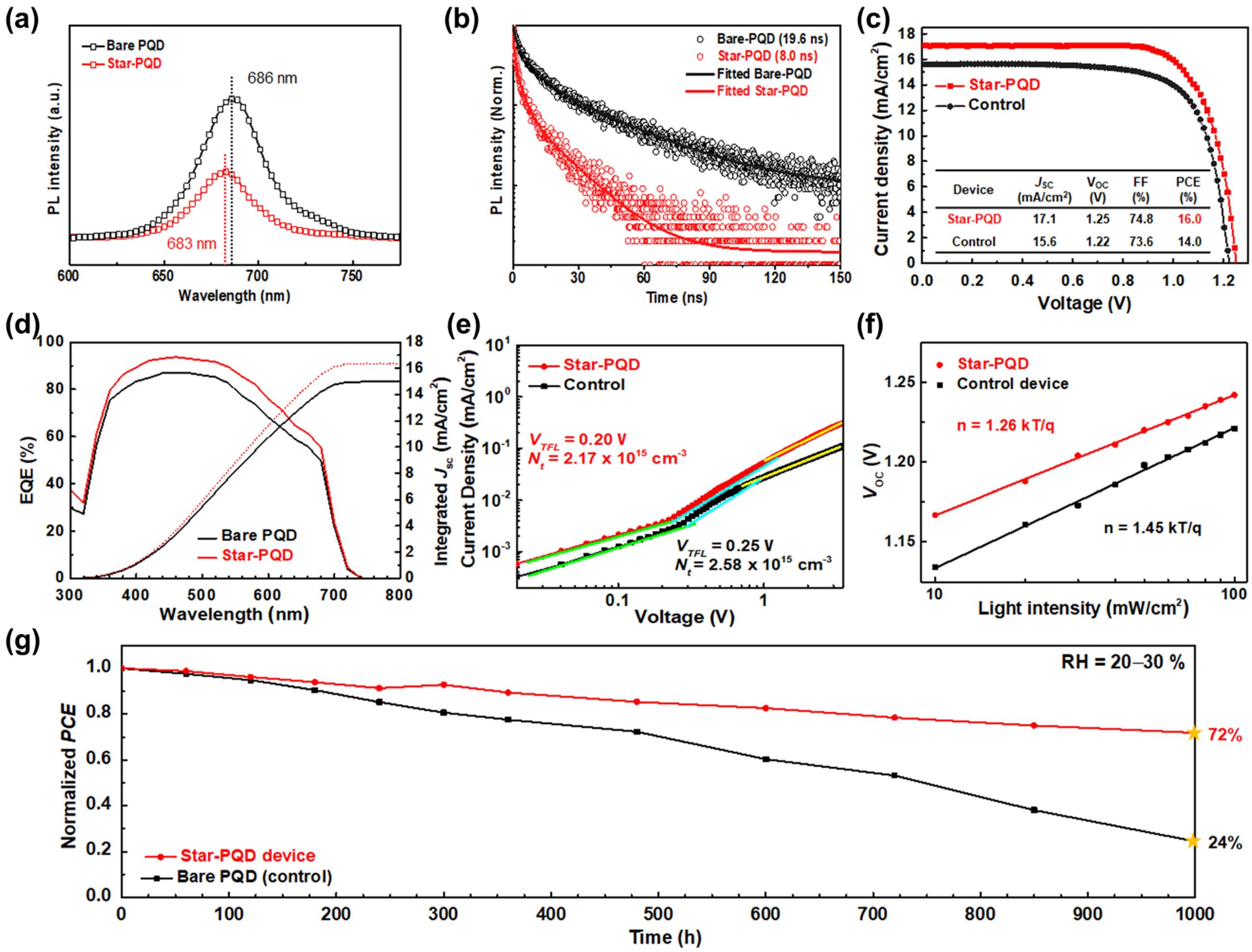

Device	J_{SC} (mA/cm²)	V_{OC} (V)	FF (%)	PCE (%)
Star-PQD	17.1	1.25	74.8	16.0
Control	15.6	1.22	73.6	14.0

Fig. 5 **a** PL spectra of glass/bare PQD and glass/Star-PQD films. **b** Time-resolved PL decay curves of the glass/bare PQD/HTM and glass/Star-PQD/HTM films. **c** Current density–voltage curves, **d** EQE spectra and integrated J_{SC} of the best performing solar cells comprising bare PQD (control) and Star-PQD films. **e** SCLC fitting results obtained from dark J–V measurements of hole-only devices compromising Star-PQD and bare PQD: trap density. **f** Light intensity-dependent V_{OC} of the Star-PQD- and bare PQD (control)-based solar cells. **g** Stability tests of solar cells fabricated from the bare PQD (control) and Star-PQD films under ambient conditions (20–30% RH)

https://doi.org/10.1007/s40820-022-00946-x

are shown in Table S2. The carrier lifetime was much shorter in the Star-PQD/Spiro-OMeTAD film (8.0 ns) than in the bare PQD/Spiro-OMeTAD film (19.6 ns). These results indicate that the favorable band alignment at the Star-PQD/Spiro-OMeTAD interface reduced the carrier recombination loss and thus improved the efficiency of hole extraction.

Finally, we fabricated $CsPbI_3$-PQD solar cells with and without Star-TrCN treatment of PQD solids (Fig. 1a). The fabrication method is described in Experimental section. The current density–voltage (*J*–*V*) curves of the Star-PQD and bare PQD-based devices are shown in Fig. 5c. The PCE of the Star-PQD-based device was improved to 16.0%, much higher than that of the bare PQD-based device (14.0%) with the same architecture and significantly higher than those of previously reported organic/$CsPbI_3$-PQD HSCs (Table S3 and Fig. S13). The enhanced PCE of the Star-PQD-based devices was attributed to the improved short-circuit current density (J_{SC}) and open-circuit voltage (V_{OC}) caused by the cascade energy band structure at the Star-PQD/HTM interface and the defect passivation effect. The photovoltaic parameters of the best performing devices are detailed in Fig. 5c (inset table). Histograms of different parameters for the device are presented in Fig. S14, which suggests the excellent reproducibility of Star-PQD-based devices. The external quantum efficiency (EQE) and integrated J_{SC} spectra are shown in Fig. 5d. The fully integrated J_{SC} values of the Star-PQD- and bare PQD-based devices were 16.4 and 15.1 mA cm^{-2}, respectively, consistent with the obtained values of the *J*–*V* measurements.

The trap-state densities obtained from the dark *J*–*V* measurements of hole-only devices comprising Star-PQD and bare PQD are shown in Fig. 5e. The Star-PQD-based device showed a lower trap-state density ($N_t = 2.17 \times 10^{15}$ cm^{-3}) than the bare PQD device ($N_t = 2.58 \times 10^{15}$ cm^{-3}), suggesting the high V_{OC} values of the Star-PQD-based device [52]. This result indicates that Star-TrCN could effectively passivate defects in $CsPbI_3$ films, in consistent with XPS and steady-state PL results. In addition, we compare hole mobility of Star-PQD and bare PQD (Fig. S15). The hole mobility (μ_h) was estimated by using the SCLC model [53]. The hole mobility of Star-PQD increased from 3.03×10^{-5} to 9.89×10^{-5} cm^2 V^{-1} s^{-1}, indicating that the Star-TrCN could effectively reduce the defect density in $CsPbI_3$ films, in consonance with XPS and steady-state PL results. The light-dependent V_{OC} measurement was performed to compare the charge carrier recombination in solar cells based on Star-PQD and bare PQD (Fig. 5f). The slope of the Star-PQD device (1.26 *kT*/*q*) was lower than that of the bare PQD device (1.45 *kT*/*q*). This result indicated that trap-assisted recombination was effectively decreased in Star-PQD devices [54]. Figure S16 shows the hysteresis behaviors of the Star-PQD- and bare PQD-based devices. The pronounced hysteresis effect in the bare PQD device was suppressed in the Star-PQD-based device. In the forward scan, the initial PCE of Star-PQD-based device was maintained up to 90%, whereas that of bare PQD-based device was maintained only up to 79%. This result indicates that charge accumulation at the PQD/HTM interface was reduced in the Star-PQD-based devices (by virtue of the efficient hole extraction ability as mentioned above). The operational device stability of the Star-PQD solar cells was demonstrated in stable power output measurements (Fig. S17). The long-term stabilities of solar cells comprising bare PQD and Star-PQD were compared after shelf storage at the same ambient conditions (25 °C, 20–30% RH) over 1000 h without additional encapsulation (Fig. 5g). The Star-PQD device was remarkably more stable than bare PQDs, consistent with our experimental results on moisture stability with and without the Star-TrCN treatment (Fig. 4). This result indicated that the Star-PQD hybrid approach improved the moisture stability of cubic-phase $CsPbI_3$-PQDs, which have an appropriate bandgap energy for single-junction solar cells. Consequently, the best performing devices in this study showed a PCE of 16.0% and retained > 72% of the initial efficiency after 1000 h.

4 Conclusions

In summary, we fabricated efficient and stable $CsPbI_3$-PQDs by combining organic conjugated molecules with PQDs. To achieve a successful hybrid system, we newly designed a 3D star-shaped semiconductor material (Star-TrCN) with an excellent geometric balance of coplanarity and distortion characteristics. The twisted 3D structure of Star-TrCN inhibits self-aggregation, increasing the compatibility between the organic semiconductors and PQDs. The Star-PQD hybrid film significantly enhances the cubic-phase stability of $CsPbI_3$-PQDs by passivating the surface defect and preventing moisture penetration through hygroscopic HTM (Spiro-OMeTAD). Consequently, the initial PCE of the HPQD device was maintained at 72% even after

1000 h. Furthermore, Star-TrCN forms a cascaded energy band structure, boosting the charge extraction efficiency and achieving 16.0% PCE. We report multifunctional 3D star-shaped organic semiconductors to enable efficient and stable PQD solar cells. This multidimensional organic semiconductor design can potentially realize commercial PQD photovoltaics.

Acknowledgements 2D-GIWAXS measurements were taken at a synchrotron radiation on the beamline 9A at the Pohang Accelerator Laboratory (PAL), Korea. This work was supported by National Research Foundation of Korea (NRF) grants funded by Ministry of Science and ICT (MSIT) (Nos. 2021R1A2C3004420, 2022M3J1A1085282, 2020R1C1C1012256 and 2020R1C1C1003214) and the NRF of Korea grant funded by the Korean Government (NRF-2019-Global Ph.D. Fellowship Program.

Funding Open access funding provided by Shanghai Jiao Tong University.

Supplementary Information The online version contains supplementary material available at https://doi.org/10.1007/s40820-022-00946-x.

References

1. N.J. Jeon, J.H. Noh, W.S. Yang, Y.C. Kim, S. Ryu et al., Compositional engineering of perovskite materials for high-performance solar cells. Nature **517**, 476 (2015). https://doi.org/10.1038/nature14133
2. M. Saliba, T. Matsui, J.Y. Seo, K. Domanski, J.P. Correa-Baena et al., Cesium-containing triple cation perovskite solar cells: improved stability, reproducibility and high efficiency. Energy Environ. Sci. **9**, 1989–1997 (2016). https://doi.org/10.1039/C5EE03874J
3. X. Liu, J. Min, Q. Chen, T. Liu, G. Pu et al., Synergy effect of a π-conjugated ionic compound: dual interfacial energy level regulation and passivation to promote V_{oc} and stability of planar perovskite solar cells. Angew. Chem. Int. Ed. **134**(11), 202117303 (2022). https://doi.org/10.1002/ange.202117303
4. H. Choi, X. Liu, H.I. Kim, D. Kim, T. Park et al., A facile surface passivation enables thermally stable and efficient planar perovskite solar cells using a novel IDTT-based small molecule additive. Adv. Energy Mater. **11**(16), 2003829 (2021). https://doi.org/10.1002/aenm.202003829
5. Z. Li, B. Li, X. Wu, S.A. Sheppard, S. Zhang et al., Organometallic-functionalized interfaces for highly efficient inverted perovskite solar cells. Science **376**(6591), 416–420 (2022). https://doi.org/10.1126/science.abm8566
6. NREL, Best research-cell efficiency chart. (2022). https://www.nrel.gov/pv/cell-efficiency.html
7. G.W. Kim, G. Kang, J. Kim, G.Y. Lee, H.I. Kim et al., Dopant-free polymeric hole transport materials for highly efficient and stable perovskite solar cells. Energy Environ. Sci. **9**, 2326–2333 (2016). https://doi.org/10.1039/C6EE00709K
8. K. Choi, J. Lee, H. Choi, G.W. Kim, H.I. Kim et al., Heat dissipation effects on the stability of planar perovskite solar cells. Energy Environ. Sci. **13**, 5059–5067 (2022). https://doi.org/10.1039/D0EE02859B
9. T.A. Berhe, W.N. Su, C.H. Chen, C.J. Pan, J.H. Cheng et al., Organometal halide perovskite solar cells: degradation and stability. Energy Environ. Sci. **9**, 323–356 (2016). https://doi.org/10.1039/C5EE02733K
10. Y. Wang, M.I. Dar, L.K. Ono, T. Zhang, M. Kan et al., Thermodynamically stabilized β-CsPbI$_3$-based perovskite solar cells with efficiencies >18%. Science **365**, 591–595 (2019). https://doi.org/10.1126/science.aav8680
11. Q. Ye, Y. Zhao, S. Mu, F. Ma, F. Gao et al., Cesium lead inorganic solar cell with efficiency beyond 18% via reduced charge recombination. Adv. Mater. **31**(49), 1905143 (2019). https://doi.org/10.1002/adma.201905143
12. K. Choi, D.H. Lee, W. Jung, S. Kim, D. Lee et al., 3D Interaction of zwitterions for highly stable and efficient inorganic CsPbI$_3$ solar cells. Adv. Funct. Mater. **32**(16), 2112027 (2021). https://doi.org/10.1002/adfm.202112027
13. M. Yue, J. Su, P. Zhao, Z. Lin, J. Zhang et al., Optimizing the performance of CsPbI$_3$-based perovskite solar cells via doping a ZnO electron transport layer coupled with interface engineering. Nano-Micro Lett. **11**, 91 (2019). https://doi.org/10.1007/s40820-019-0320-y
14. A. Marronnier, G. Roma, S. Boyer-Richard, L. Pedesseau, J.M. Jancu et al., Anharmonicity and disorder in the black phases of cesium lead iodide used for stable inorganic perovskite solar cells. ACS Nano **12**(4), 3477–3486 (2018). https://doi.org/10.1021/acsnano.8b00267
15. A. Swarnkar, A.R. Marshall, E.M. Sanehira, B.D. Chernomordik, D.T. Moore et al., Quantum dot–induced phase stabilization of α-CsPbI$_3$ perovskite for high-efficiency photovoltaics. Science **354**, 92–95 (2016). https://doi.org/10.1126/science.aag2700

16. Q. Zhao, A. Hazarika, L.T. Schelhas, J. Liu, E.A. Gaulding et al., Size-dependent lattice structure and confinement properties in $CsPbI_3$ perovskite nanocrystals: negative surface energy for stabilization. ACS Energy Lett. **5**(1), 238–247 (2020). https://doi.org/10.1021/acsenergylett.9b02395
17. M.T. Hoang, A.S. Pannu, Y. Yang, S. Madani, P. Shaw et al., Surface treatment of inorganic $CsPbI_3$ nanocrystals with guanidinium iodide for efficient perovskite light-emitting diodes with high brightness. Nano-Micro Lett. **14**, 69 (2022). https://doi.org/10.1007/s40820-022-00813-9
18. S. Lim, G. Lee, S. Han, J. Kim, S. Yun et al., Monodisperse perovskite colloidal quantum dots enable high-efficiency photovoltaics. ACS Energy Lett. **6**(6), 2229–2237 (2021). https://doi.org/10.1021/acsenergylett.1c00462
19. X. Zhang, H. Huang, X. Ling, J. Sun, X. Jiang et al., Homojunction perovskite quantum dot solar cells with over 1 µm-thick photoactive layer. Adv. Mater. **34**(2), 2105977 (2022). https://doi.org/10.1002/adma.202105977
20. J. Yuan, X. Zhang, J. Sun, R. Patterson, H. Yao et al., Hybrid perovskite quantum dot/non-fullerene molecule solar cells with efficiency over 15%. Adv. Funct. Mater. **31**(27), 2101272 (2021). https://doi.org/10.1002/adfm.202101272
21. A. Pan, B. He, X. Fan, Z. Liu, J.J. Urban et al., Insight into the ligand-mediated synthesis of colloidal $CsPbBr_3$ perovskite nanocrystals: the role of organic acid, base, and cesium precursors. ACS Nano **10**(8), 7943–7954 (2016). https://doi.org/10.1021/acsnano.6b03863
22. Y. Wang, J. Yuan, X. Zhang, X. Ling, B.W. Larson et al., Surface ligand management aided by a secondary amine enables increased synthesis yield of $CsPbI_3$ perovskite quantum dots and high photovoltaic performance. Adv. Mater. **32**(32), 2000449 (2020). https://doi.org/10.1002/adma.202000449
23. L. Duan, L. Hu, X. Guan, C.H. Lin, D. Chu et al., Quantum dots for photovoltaics: a tale of two materials. Adv. Energy Mater. **11**(20), 2100354 (2021). https://doi.org/10.1002/aenm.202100354
24. J. Khan, X. Zhang, J. Yuan, Y. Wang, G. Shi et al., Tuning the surface-passivating ligand anchoring position enables phase robustness in $CsPbI_3$ perovskite quantum dot solar cells. ACS Energy Lett. **5**(10), 3322–3329 (2020). https://doi.org/10.1021/acsenergylett.0c01849
25. S. Lim, J. Kim, J.Y. Park, J. Min, S. Yun et al., Suppressed degradation and enhanced performance of $CsPbI_3$ perovskite quantum dot solar cells via engineering of electron transport layers. ACS Appl. Mater. Interfaces **13**(5), 6119–6129 (2021). https://doi.org/10.1021/acsami.0c15484
26. J. Duan, Y. Wang, X. Yang, Q. Tang, Alkyl-chain-regulated charge transfer in fluorescent inorganic $CsPbBr_3$ perovskite solar cells. Angew. Chem. Int. Ed. **59**(11), 4391–4395 (2020). https://doi.org/10.1002/anie.202000199
27. K. Hills-Kimball, H. Yang, T. Cai, J. Wang, O. Chen, Recent advances in ligand design and engineering in lead halide perovskite nanocrystals. Adv. Sci. **8**(12), 2100214 (2021). https://doi.org/10.1002/advs.202100214
28. A. Shrestha, M. Batmunkh, A. Tricoli, S.Z. Qiao, S. Dai, Near-infrared active lead chalcogenide quantum dots: preparation, post-synthesis ligand exchange, and applications in solar cells. Angew. Chem. Int. Ed. **58**(16), 5202–5224 (2019). https://doi.org/10.1002/anie.201804053
29. Q. Wang, Z. Jin, D. Chen, D. Bai, H. Bian et al., µ-Graphene crosslinked $CsPbI_3$ quantum dots for high efficiency solar cells with much improved stability. Adv. Energy Mater. **8**(22), 1800007 (2018). https://doi.org/10.1002/aenm.201800007
30. Z.H. Bakr, Q. Wali, A. Fakharuddin, L. Schmidt-Mende, T.M. Brown et al., Advances in hole transport materials engineering for stable and efficient perovskite solar cells. Nano Energy **34**, 271–305 (2017). https://doi.org/10.1016/j.nanoen.2017.02.025
31. L. Zhang, C. Liu, J. Zhang, X. Li, C. Cheng et al., Intensive exposure of functional rings of a polymeric hole-transporting material enables efficient perovskite solar cells. Adv. Mater. **30**(39), 1804028 (2018). https://doi.org/10.1002/adma.201804028
32. J. Yuan, X. Ling, D. Yang, F. Li, S. Zhou et al., Band-aligned polymeric hole transport materials for extremely low energy loss α-$CsPbI_3$ perovskite nanocrystal solar cells. Joule **2**, 2450–2463 (2018). https://doi.org/10.1016/j.joule.2018.08.011
33. K. Ji, J. Yuan, F. Li, Y. Shi, X. Ling et al., High-efficiency perovskite quantum dot solar cells benefiting from a conjugated polymer-quantum dot bulk heterojunction connecting layer. J. Mater. Chem. A **8**, 8104–8112 (2020). https://doi.org/10.1039/D0TA02743J
34. S. Lim, S. Han, D. Kim, J. Min, J. Choi et al., Key factors affecting the stability of $CsPbI_3$ perovskite quantum dot solar cells: a comprehensive review. Adv. Mater. (2022). https://doi.org/10.1002/adma.202203430
35. B. Chen, P.N. Rudd, S. Yang, Y. Yuan, J. Huang, Imperfections and their passivation in halide perovskite solar cells. Chem. Soc. Rev. **48**, 3842–3867 (2019). https://doi.org/10.1039/C8CS00853A
36. L. Hu, Q. Zhao, S. Huang, J. Zheng, X. Guan et al., Flexible and efficient perovskite quantum dot solar cells via hybrid interfacial architecture. Nat. Commun. **12**, 466 (2021). https://doi.org/10.1038/s41467-020-20749-1
37. J. Yuan, A. Gallagher, Z. Liu, Y. Sun, W. Ma, High-efficiency polymer–PbS hybrid solar cells via molecular engineering. J. Mater. Chem. A **3**, 2572–2579 (2015). https://doi.org/10.1039/C4TA03995E
38. S. Holliday, R.S. Ashraf, C.B. Nielsen, M. Kirkus, J.A. Rohr et al., A rhodanine flanked nonfullerene acceptor for solution-processed organic photovoltaics. J. Am. Chem. Soc. **137**(2), 898–904 (2015). https://doi.org/10.1021/ja5110602
39. W. Wu, G. Zhang, X. Xu, S. Wang, Y. Li et al., Wide bandgap molecular acceptors with a truxene core for efficient nonfullerene polymer solar cells: linkage position on molecular configuration and photovoltaic properties. Adv. Funct. Mater. **28**(18), 1707493 (2018). https://doi.org/10.1002/adfm.201707493
40. D.H. Lee, D.H. Kim, T. Kim, D.C. Lee, S. Cho et al., Solid-solvent hybrid additive for the simultaneous control of the macro- and micro-morphology in non-fullerene-based organic

solar cells. Nano Energy **93**, 106878 (2022). https://doi.org/10.1016/j.nanoen.2021.106878

41. Y. Wang, G. Chen, D. Ouyang, X. He, C. Li et al., High phase stability in $CsPbI_3$ enabled by Pb–I octahedra anchors for efficient inorganic perovskite photovoltaics. Adv. Mater. **32**(24), 2000186 (2020). https://doi.org/10.1002/adma.202000186
42. J. Wang, J. Zhang, Y. Zhou, H. Liu, Q. Xue et al., Highly efficient all-inorganic perovskite solar cells with suppressed non-radiative recombination by a Lewis base. Nat. Commun. **11**, 177 (2020). https://doi.org/10.1038/s41467-019-13909-5
43. Q. Cao, Y. Li, H. Zhang, J. Yang, J. Han et al., Efficient and stable inverted perovskite solar cells with very high fill factors via incorporation of star-shaped polymer. Sci. Adv. **7**, eabg0633 (2021). https://doi.org/10.1126/sciadv.abg0633
44. L. Mester, A.A. Govyadinov, S. Chen, M. Goikoetxea, R. Hillenbrand, Subsurface chemical nanoidentification by nano-FTIR spectroscopy. Nat. Commun. **11**, 3359 (2020). https://doi.org/10.1038/s41467-020-17034-6
45. S. Han, L. Guan, T. Yin, J. Zhang, J. Guo et al., Unveiling the roles of halogen ions in the surface passivation of $CsPbI_3$ perovskite solar cells. Phys. Chem. Chem. Phys. **24**, 10184–10192 (2020). https://doi.org/10.1039/D2CP00109H
46. L. Long, D. Cao, J. Fei, J. Wang, Y. Zhou et al., Effect of surface intrinsic defects on the structural stability and electronic properties of the all-inorganic halide perovskite $CsPbI_3$ (001) film. Chem. Phys. Lett. **734**, 136719 (2019). https://doi.org/10.1016/j.cplett.2019.136719
47. F. Li, J. Yuan, X. Ling, Y. Zhang, Y. Yang et al., A universal strategy to utilize polymeric semiconductors for perovskite solar cells with enhanced efficiency and longevity. Adv. Funct. Mater. **28**(15), 1706377 (2018). https://doi.org/10.1002/adfm.201706377
48. Y. Liu, L. Zhang, S. Chen, C. Liu, Y. Li et al., Water-soluble conjugated polyelectrolyte hole transporting layer for efficient sky-blue perovskite light-emitting diodes. Small **17**(37), 2101477 (2021). https://doi.org/10.1002/smll.202101477
49. J. Xue, R. Wang, L. Chen, S. Nuryyeva, T.H. Han et al., A small-molecule “charge driver” enables perovskite quantum dot solar cells with efficiency approaching 13%. Adv. Mater. **31**(37), 1900111 (2019). https://doi.org/10.1002/adma.201900111
50. Q. Cao, J. Yang, T. Wang, Y. Li, X. Pu et al., Star-polymer multidentate-cross-linking strategy for superior operational stability of inverted perovskite solar cells at high efficiency. Energy Environ. Sci. **14**, 5406–5415 (2021). https://doi.org/10.1039/D1EE01800K
51. X. Liao, Q. Xie, Y. Guo, Q. He, Z. Chen et al., Inhibiting excessive molecular aggregation to achieve highly efficient and stabilized organic solar cells by introducing a star-shaped nitrogen heterocyclic-ring acceptor. Energy Environ. Sci. **15**, 384–394 (2022). https://doi.org/10.1039/D1EE02858H
52. W. Dong, W. Qiao, S. Xiong, J. Yang, X. Wang et al., Surface passivation and energetic modification suppress nonradiative recombination in perovskite solar cells. Nano-Micro Lett. **14**, 108 (2022). https://doi.org/10.1007/s40820-022-00854-0
53. G.G. Malliaras, J.R. Salem, P.J. Brock, C. Scott, Electrical characteristics and efficiency of single-layer organic light-emitting diodes. Phys. Rev. B **58**, R13411 (1998). https://doi.org/10.1103/PhysRevB.58.R13411
54. E. Yassitepe, Z. Yang, O. Voznyy, Y. Kim, G. Walters et al., Amine-free synthesis of cesium lead halide perovskite quantum dots for efficient light-emitting diodes. Adv. Funct. Mater. **26**(47), 8757–8763 (2016). https://doi.org/10.1002/adfm.201604580